The Astrophysical Journal, 982:202 (8pp), 2025 April 1 https://doi.org/10.3847/1538-4357/adb8d6

Determining the Polarization of a Coronal Standing Kink Oscillation Using Spectral Imaging Techniques with CoMP

T. J. Duckenfield[1,2], D. B. Jess[1,3], R. J. Morton[2], and S. Jafarzadeh[1]
[1] Astrophysics Research Centre, School of Mathematics and Physics, Queen's University Belfast, Belfast BT7 1NN, UK; t.duckenfield@qub.ac.uk
[2] Department of Mathematics, Physics and Electrical Engineering, Northumbria University, Newcastle upon Tyne NE1 8ST, UK
[3] Department of Physics and Astronomy, California State University Northridge, USA

Received 2025 February 1; revised 2025 February 17; accepted 2025 February 20; published 2025 March 31

Abstract

Coronal oscillations offer insight into energy transport and driving in the solar atmosphere. Knowing its polarization state helps constrain a wave's displacement and velocity amplitude, improving estimates of wave energy flux and deposition rate. We demonstrate a method to combine imaging and spectral data to infer the polarization of a coronal loop's standing kink wave, without the need for multiple instruments or multiple lines of sight. We use the unique capabilities of the Coronal Multi-channel Polarimeter (CoMP) to observe the standing kink mode of an off-limb coronal loop perturbed by an eruption. The full off-disk corona is observed using the 1074 nm Fe XIII spectral line, providing Doppler velocity, intensity, and line width. By tracking the oscillatory motion of a loop apex in a time–distance map, we extract the line-of-sight (Doppler) velocity of the inhomogeneity as it sways and compare it with the derivative of its plane-of-sky displacement. This analysis provides the loop's velocity in two perpendicular planes as it oscillates with a period of $8.9^{+0.5}_{-0.5}$ minutes. Through detailed analysis of the phase relation between the transverse velocities, we infer the kink oscillation to be horizontally polarized, oscillating in a plane tilted $-13\overset{\circ}{.}6^{+2.9}_{-3.0}$ away from the plane of sky. The line widths show a periodic enhancement during the kink oscillation, exhibiting both the kink period and its double. This study is the first to combine direct imaging and spectral data to infer the polarization of a coronal loop oscillation from a single viewpoint.

Unified Astronomy Thesaurus concepts: Active solar corona (1988); Solar oscillations (1515); Infrared spectroscopy (2285); Solar coronal seismology (1994)

Materials only available in the online version of record: animations

1. Introduction

The solar corona is a highly dynamic environment, hosting a wide range of wave phenomena that can be used to probe the local plasma conditions (V. M. Nakariakov et al. 2024). Among these, magnetohydrodynamic kink oscillations are particularly useful, due to their widespread occurrence and well-established ability to probe the magnetic and density structuring of their host inhomogeneities across the solar atmosphere, such as coronal loops, prominences, fibrils, and spicules (see the recent reviews of V. M. Nakariakov et al. 2021; D. B. Jess et al. 2023). These collective transverse motions of a (typically density-enhanced) cylinder are characterized by an azimuthal wavenumber m equal to 1 (M. S. Ruderman & R. Erdélyi 2009). The phase speed of the wave is equal to the kink speed, C_K, which is a density-weighted average of the Alfvén speed across the inhomogeneity. Coronal loops often exhibit kink oscillations, and since there is wave reflection at the loop footpoints at the much denser transition region and chromosphere, a longitudinal standing mode (and its higher harmonics) is often formed. The period of the nth longitudinal harmonic is determined by the loop length, L, following the relationship $P = 2L/(nC_K)$ (V. M. Nakariakov et al. 2024). The excitation of these longitudinal harmonics is governed by the characteristics of the driver (I. V. Zimovets & V. M. Nakariakov 2015). However, higher harmonics damp more rapidly and require greater spatial and temporal resolution to detect, resulting in most observations of standing kink oscillations being related to the fundamental mode.

Kink modes may be damped extremely quickly (in a matter of a few periods) through the process of resonant absorption (M. Goossens et al 2002; D. J. Pascoe et al. 2016; M. Guo et al. 2020; R. J. Morton et al. 2021). The bulk motion of the plasma within the loop cross section couples to localized Alfvénic motions at a particular radius where $C_K = v_A(r)$, since the cross-sectional inhomogeneity leads to a radially varying Alfvén speed. These internal motions remove energy from the kink oscillation and lead to strong damping, usually with a quality factor (ratio of damping time to period) of ∼1–10. The connection between standing kink oscillations and the local plasma parameters has been extensively exploited to diagnose the coronal plasma via coronal seismology (V. M. Nakariakov et al. 2024).

Transverse oscillations of coronal loops can have two linear polarizations—a vertical polarization indicates motion in a plane perpendicular to the solar surface, while horizontal polarization corresponds to displacement parallel to the surface. In addition, transverse oscillations of coronal loops can exhibit elliptical or circular polarization indicative of coupled displacements in both vertical and horizontal directions, resulting in a rotational or helical motion of the loop's axis. The damping by resonant absorption is independent of whether the wave is linearly, circularly, or elliptically polarized (N. Magyar et al. 2022). However, determining the wave polarization allows more accurate constraints on its true displacements and velocity amplitudes. This directly improves estimates of wave energy fluxes and deposition rates, which are of crucial importance for assessing the contribution of waves to coronal heating and the transport of energy through the atmosphere.

In coronal loop observations, the majority of kink modes are thought to be in the horizontal polarization mode, excited by eruptive events (e.g., I. Ballai et al. 2011; I. V. Zimovets & V. M. Nakariakov 2015). The prevalence of horizontal modes is presumably because a general excitation mechanism, such as an eruption, is more likely to impact the loop from the side, rather than below/above. Indeed, the recent work by S. Zhong et al. (2023) determined the horizontal (or weakly oblique) polarization of a large-scale kink mode utilizing the perspective of multiple instruments. Vertically polarized modes have been detected in individual cases, for example in E. Verwichte et al. (2009) and M. J. Aschwanden & C. J. Schrijver (2011). However, the need for multiple perspectives to determine polarization limits studies, as it requires the same oscillation event to be seen by two different instruments. Moreover, without a priori knowledge of the line-of-sight (LOS) angle, there is no unambiguous signature of the polarization state in the forward-modeled Doppler velocities from the induced internal flows (M. Goossens et al. 2014).

In this work, we demonstrate a novel method for inferring the polarization of a specific loop oscillation by analyzing its velocity phase portrait, combining observations of the loop's transverse motion in the plane of the sky with the corresponding LOS Doppler velocities. Unlike traditional approaches that require stereoscopic observations from multiple viewpoints, this technique enables the characterization of an oscillation's polarization using data from a single instrument.

2. Observations

2.1. Coronal Multi-channel Polarimeter

The Coronal Multi-channel Polarimeter instrument (CoMP; S. Tomczyk et al. 2008) is a ground-based instrument designed to observe the solar corona that operated from the Mauna Loa Solar Observatory in Hawaii from 2013 to 2018. At a subminute cadence, occulted images are taken of the solar corona, and at each pixel a spectrum is extracted with particular targeting of the "forbidden" Fe XIII 1074.7 and 1079.8 nm near-infrared spectral lines. These spectral profiles are fitted with Gaussian functions to determine the Doppler velocity and line intensity, and the intensity ratio can be used to map the coronal electron number density (which, assuming overall charge neutrality, can indicate plasma density, e.g., Z. Yang et al. 2020).

While CoMP is a powerful tool for studying solar dynamics, there is a well-documented tendency for spectrometers observing coronal lines to underestimate Doppler velocities. This underestimation is due to the physics of radiative transfer through optically thin plasmas, in addition to the superposition of out-of-phase oscillations along the LOS, which can broaden spectral lines and diminish the measured velocity amplitudes (S. W. McIntosh & B. D. Pontieu 2012; I. D. Moortel & D. J. Pascoe 2012; R. J. Morton et al. 2015; V. Pant et al. 2019), especially in the quiet Sun. Being optically thin, the 1074 nm emission used in these observations is weighted toward the higher-density plasma, which in our case is ideal since we are interested in the more dense active region loop. Additionally, kink oscillations in active regions are coherent over spatial scales larger than CoMP's resolution (R. Sharma & R. J. Morton 2023), allowing the loop to stand out against its surroundings when integrated along the LOS. However, it is important to consider the potential systematic uncertainty in the Doppler velocities. A recent study (J.-O. Lee et al. 2021) compared Hinode/EUV Imaging Spectrometer (EIS) data with CoMP 1074 nm observations and found that while the line widths and Doppler velocities are generally correlated, in bright active region structures the EIS Doppler velocities are larger than CoMP's absolute values by a factor of ∼1.5.

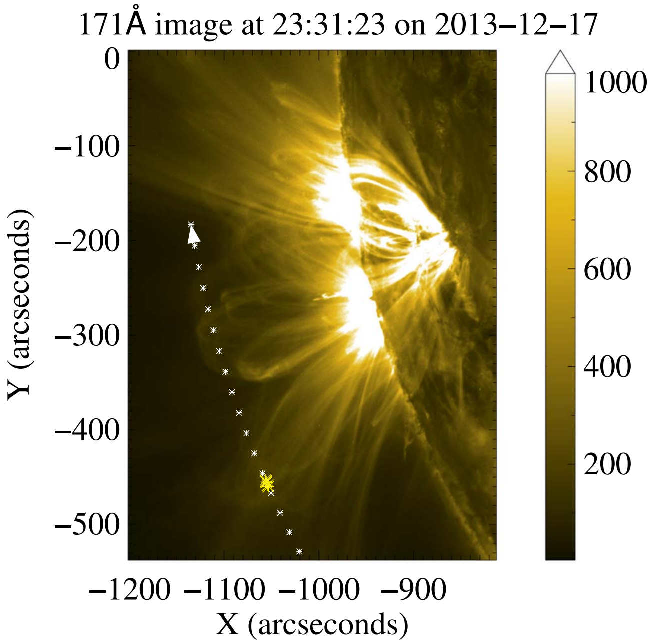

Figure 1. Active Region 11925 observed by the Solar Dynamics Observatory's Atmospheric Imaging Assembly in the 171 Å channel. The white dashed line represents a slit positioned parallel to the solar surface at a radius of 1.18 $R_\odot$. The yellow points trace the measured displacement of the oscillating feature studied. The animation shows the evolution from 23:20:11 on 2013 December 17 until 00:29:59 on 2013 December 18. The real-time duration of the animation is 17 s.

(An animation of this figure is available in the online article.)

Previous work using CoMP data has shown an abundance of propagating Alfvénic waves propagating both inward and out of the corona, which appear only weakly damped (R. J. Morton et al. 2021) and have a transverse correlation length of 7.6–9.3 Mm, associated with supergranulation (R. Sharma & R. J. Morton 2023). Using the propagation speed of these waves, combined with the density estimate from the Fe XIII forbidden line ratio, global maps of the coronal magnetic field can be made (Z. Yang et al. 2024).

2.2. Event Description

To demonstrate the ability of the CoMP instrument in combining Doppler velocity and imaging, we consider an off-limb large-scale kink oscillation observed on 2013 December 17. There is a minor eruption off the eastern solar limb commencing around 23:25, perturbing a bundle of coronal loops (associated with NOAA Active Region 11925) that causes large-amplitude transverse oscillations that last approximately 40 minutes, as seen in Solar Dynamics Observatory/Atmospheric Imaging Assembly (SDO/AIA) 193 Å and 171 Å (Figure 1). The CoMP instrument was running nearly continuously at 30 s cadence from 23:21 onward, capturing the eruption in the 1074 nm line only. The 1079 nm line information is unavailable, and due to the absence of line intensity ratio measurements, traditional magnetoseismology methods commonly applied with CoMP

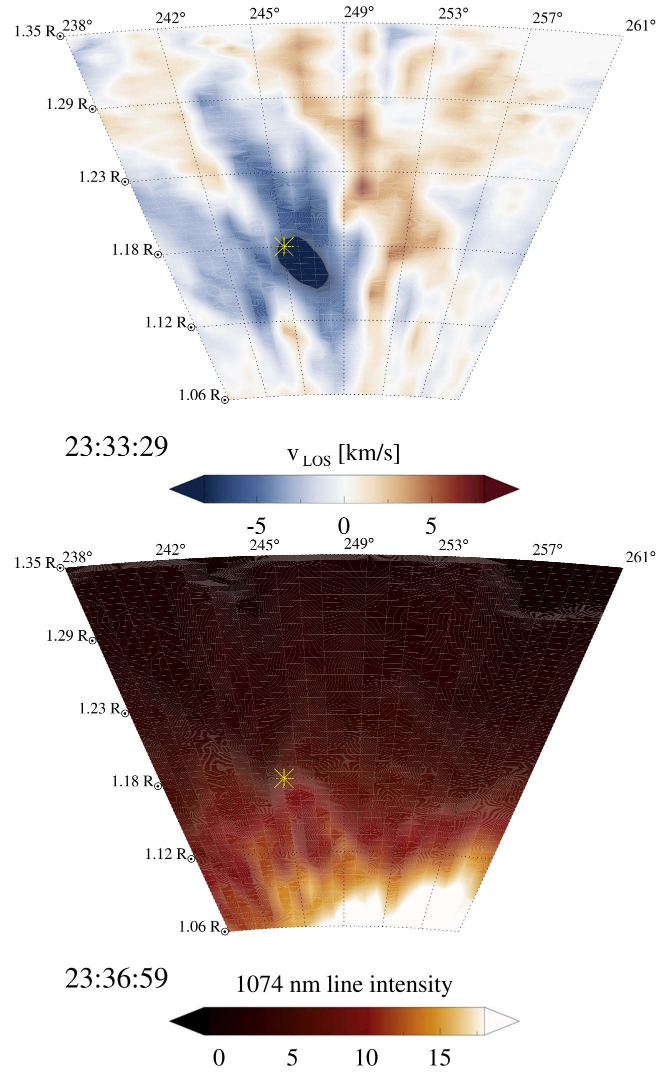

Figure 2. Plots showing Doppler velocity (top) and line intensity (bottom) measured by CoMP as the eruption propagates outward. The angular extent is 220°–270° measured clockwise from solar north and covers a radial range from 1.06 to 1.35 $R_\odot$. The top plot shows a blueshifted loop apex (marked with a yellow cross) superimposed on a background of redshifted plasma from the erupting material. The bottom plot, separated by approximately 4 minutes (roughly half the oscillation period), reveals the full extent of the loop of interest, including its legs. The animation shows the eruption from 23:21:29 until 00:00:29 the next day. The real-time duration of the animation is 5 s.

(An animation of this figure is available in the online article.)

data (such as in Z. Yang et al. 2020) are not feasible in this case. Remarkably, despite this limitation, it remains possible to deduce the polarization state of the oscillation using only a single line profile, showcasing the robustness of CoMP's capabilities in diagnosing oscillatory phenomena. From the 1074 nm profile, fitted by a three-point Gaussian, maps of intensity, Doppler velocity, and line widths are found.

The region of the corona in the CoMP data that is visibly affected by the eruption is shown in Figure 2. The erupted material appears on this plot as a column of redshifted plasma, with minimal intensity perturbations in this bandpass, moving radially outward and crossing a distance of 1.06 solar radii at approximately 255°.

While the SDO/AIA data depict a multitude of loops in this region, most of which are perturbed by the eruption, in the CoMP 1074 nm data only one coronal loop is easily discernable in the intensity image foreground. At this loop's apex, marked by a yellow point at its equilibrium position (−1054″, −454″), strong and periodic LOS velocities are observed, also evident in the loop legs to a lesser extent.

For this event, detailed investigation found that the maximum displacement in the plane of the sky aligns with the azimuthal direction. In the general case, tracking loop motion along both azimuthal and radial directions within the plane of the sky is ideal to fully capture the loop's dynamics. However, in this specific case, radial displacement is negligible. Thus, comparing the azimuthal displacement with the LOS velocity provides sufficient information to determine the loop's polarization state.

A series of azimuthal slits approximately 500″ long and parallel to the solar surface were made from 1.06 to 1.35 $R_\odot$ in increments of 0.01 $R_\odot$, centered at 250° from solar north (clockwise) to capture the eruption and subsequent oscillation. From these slits time–distance maps were extracted, such as those shown in Figure 3. The most prominent oscillatory signal in the CoMP data is visible at the loop apex, which corresponds to a height of 1.18 $R_\odot$ and angle from solar north of 246°.

2.3. Fitting Loop Displacement

To compare LOS velocity with plane-of-sky (POS) motion, we must precisely map the displacement of a specific inhomogeneity (loop). Previous studies have often relied on manual selection of loop positions or simple Gaussian fitting of intensity structures, but these approaches are insufficient for this study, as we are primarily interested in the derivative of displacement. Minor inaccuracies in displacement would be amplified in its derivative. To ensure a precise fit, we use the Solar Bayesian Analysis Toolkit (SoBaT; S. A. Anfinogentov et al. 2021), employing Bayesian inference and Markov Chain Monte Carlo (MCMC) sampling to model the intensity profile across the time–distance map with a density enhancement plus background. Detailed modeling of LOS integrated density enhancements can be found in D. J. Pascoe et al. (2016).

We focus on the time–distance map for the azimuthal slit at 1.18 $R_\odot$, which aligns most closely with the loop apex and therefore shows the clearest transverse motion signature, seen in Figure 3. Direct fitting to the (raw) intensity map in panel (a) proved unreliable. Fortunately, the feature seen at ≈80 Mm is a distinct intensity dip, providing excellent contrast to the overlying, less well-defined loop structure at ≈100 Mm. We exploit this by fitting the displacement of the loop's "shadow," which exhibits a profile more amenable for our fitting procedure, followed by a shift based on the fitted radius. By using a Bayesian framework with SoBaT, we simultaneously optimize for both the displacement and the radius by marginalizing the joint posterior distribution for each parameter. This accounts for uncertainties in other parameters, allowing the track fitted on the observed "shadow" to be aligned onto the density enhancement, seen clearly in Figure 4. The difficulty of fitting a simple profile directly to the broad, non-Gaussian intensity feature at ∼100 Mm is apparent when considering the red curve (original data). Conversely, fitting the inverted and (spatially) edge-filtered data, represented by the black curve, is more reliable and precise, as demonstrated by the closeness of the dashed light-blue curve. To track the position of the intensity enhancement (loop of interest), we apply a shift based on the fitted curve width, with an average shift of approximately 27 Mm. This results in the solid blue curve in Figure 4,

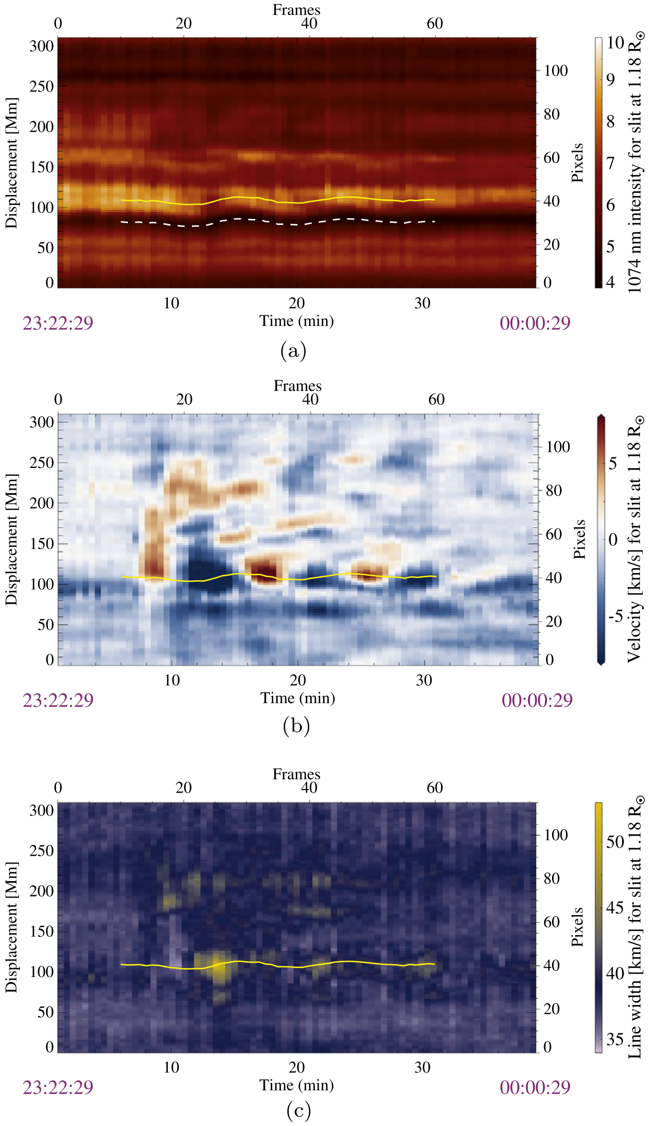

Figure 3. Time–distance plots for the slit parallel to the solar surface at 1.18 $R_{\odot}$, i.e., approximately 125.23 Mm above the limb, between angles 238° and 260° clockwise from solar north. Panel (a) shows 1074 nm line intensity; (b) Doppler velocity; (c) line width.

from which we extract the peak position, and connecting each peak in time results in the yellow curves in Figure 3.

The derivative of the displacement in the POS is found using a Savitsky–Golay filter of the first order, and we call this the POS velocity, v_{POS}. Due to the azimuthal direction of the originating slit, the measured spatial shift and v_{POS} are the displacement and velocity in the direction parallel to the surface projected onto the POS.

2.4. Line-of-sight Velocity

Through precise tracking of the loop apex's trajectory on a time–distance map and mapping into the CoMP field of view, we determine the LOS Doppler velocity measured at the apex at each moment in time as it moves through space. The resulting Doppler velocity time series may be seen in Figure 5.

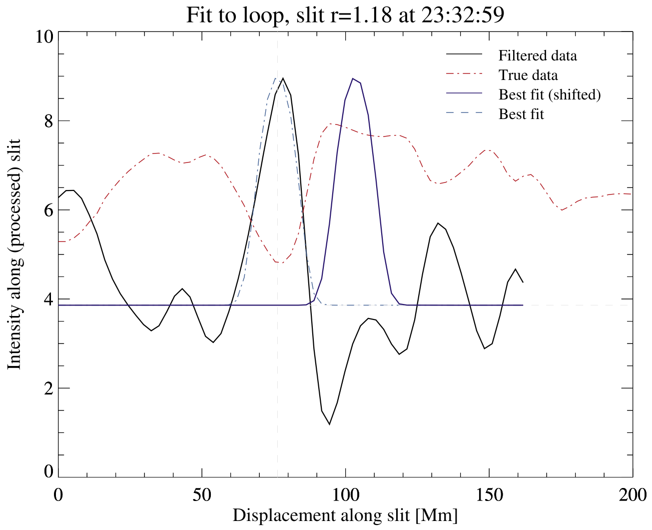

Figure 4. Plot showing how the fitted density enhancement (blue) relates to the original data (red) and the processed time series (black) on which it was calculated. The processed data have been inverted and an edge filter (in the spatial direction) applied. The fitting to the well-contrasted trough (now peak) is shown in dashed blue. The shift from dashed blue line to solid blue line has accounted for the inversion and lies within the region of high intensity (the inhomogeneity of interest). The animation shows the fit for each time step between 23:27 and 23:47. The real-time duration of the animation is 8 s.

(An animation of this figure is available in the online article.)

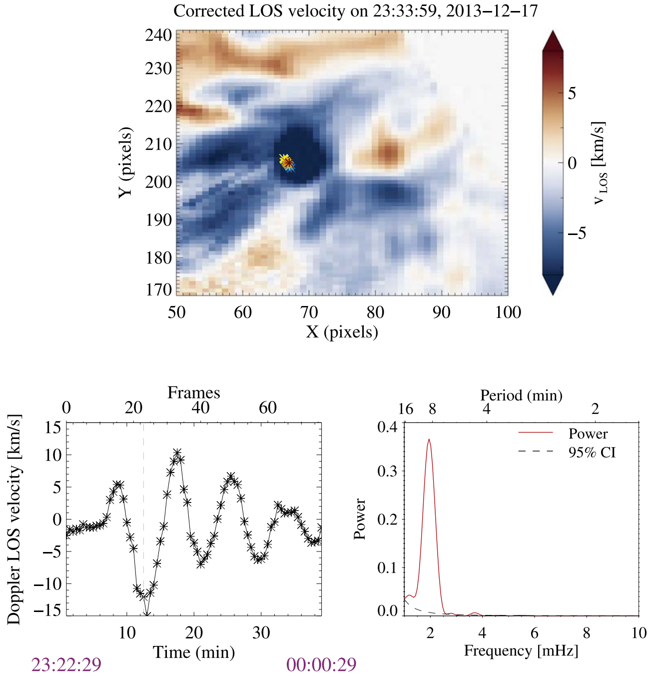

Figure 5. The Doppler velocity at the loop apex is tracked as it moves. (Top) The location of the points from which the line-of-sight velocity v_{LOS} is extracted. At this scale, these points overlap. (Bottom left) The time series v_{LOS} starting from the time of eruption, revealing a clearly sinusoidal signal. The dashed vertical line indicates the snapshot displayed above, chosen to be at a velocity oscillation maximum. (Bottom right) The power spectrum of the extracted velocity, with a peak at 2.1 mHz.

As a comparison, spectroscopic analysis of Solar Orbiter STIX data and the Hinode/EIS spectrograph found the three-dimensional reconstructed plasma flow velocities in steady, unperturbed coronal loops to be of the order $\lesssim 5\,\mathrm{km\,s^{-1}}$ and under (see Table 3, O. Podladchikova et al. 2021). The measured Doppler velocity amplitude for this oscillating loop comfortably exceeds this rest value and matches well the estimated velocity amplitudes of up to $16\,\mathrm{km\,s^{-1}}$ reported in D. M. Long et al. (2017) for a similarly excited loop.

3. Results

3.1. Oscillation Parameters

The displacement was modeled using 10^5 MCMC samples, fitting a sinusoidal function with Gaussian damping to represent the observed impulsive excitation. The functional form fitted and the best-fitting parameters of initial (projected) displacement amplitude ($-7.0^{+1.3}_{-1.4}$ Mm), period ($8.9^{+0.5}_{-0.5}$ minutes), quality factor ($1.9^{+0.5}_{-0.3}$), and offset ($109^{+0.6}_{-0.5}$ Mm) are presented in Equation (1):

$$\begin{aligned} s(t) \;=\; & -7.0^{+1.3}_{-1.4}\ [\mathrm{km\ s^{-1}}](\mathrm{amplitude}) \\ & \times \sin\left(\frac{2\pi}{8.9^{+0.5}_{-0.5}\ [\mathrm{minutes}]}t\right)(\mathrm{period}) \\ & \times \exp\left(\frac{-t^2}{(2\times(1.9^{+0.5}_{-0.3}\times 8.9^{+0.5}_{-0.5})^2)}\right)(\mathrm{damping}) \\ & +109^{+0.6}_{-0.5}\ [\mathrm{Mm}](\mathrm{offset}). \end{aligned} \tag{1}$$

Similarly, the Doppler velocity, v_{LOS}, is modeled using a Gaussian damped cosine with the same framework, whose functional form and best-fitting parameters are presented in Equation (2), yielding an initial velocity amplitude of $10.9^{+1.6}_{-1.7}$ km s^{-1} and a derived period of $8.5^{+0.5}_{-0.5}$ minutes with a quality factor just exceeding 2:

$$\begin{aligned} v_{\mathrm{LOS}} = \; & 10.9^{+1.6}_{-1.7}\ [\mathrm{km\ s^{-1}}]\ (\mathrm{amplitude}) \\ & \times \cos\left(\frac{2\pi}{8.5^{+0.5}_{-0.5}\ [\mathrm{minutes}]}t\right)(\mathrm{period}) \\ & \times \exp\left(\frac{-t^2}{(2\times(2.7^{+0.6}_{-0.4}\times 8.5^{+0.5}_{-0.5})^2)}\right)(\mathrm{damping}) \\ & -1.4^{+0.5}_{-0.5}\ [\mathrm{km\ s^{-1}}]\ (\mathrm{offset})\,. \end{aligned} \tag{2}$$

There are minor discrepancies in quality factor and period because of the short signal length, slight differences in the time series used for the respective fits, and the modeling of the same oscillation from different perspectives.

3.2. Comparison between Doppler Velocity and Displacement

The impulsively driven kink mode oscillation is pronounced in both the Doppler LOS velocity, v_{LOS}, and the azimuthal displacement in the POS (Figure 6). Both velocities exhibit a monochromatic oscillation with a common periodicity of $8.5^{+0.5}_{-0.5}$ minutes. The derivative of azimuthal displacement, v_{POS}, is nearly in antiphase with v_{LOS}, as indicated by a strong correlation coefficient of -0.89. Note that the sign of v_{POS} depends on the (arbitrary) choice of azimuthal slit direction; if the slit was chosen to be oriented in the opposite direction (e.g., north to south, not south to north), the sign of v_{POS} would reverse, resulting in in-phase velocities (positive cross correlation at zero lag). The dynamics remain consistent: v_{POS} and v_{LOS} reach their maximal magnitudes simultaneously, and both velocities are (approximately) zero when the loop reaches its maximum displacement from equilibrium. Noting that radial displacement was found to be negligible, this behavior confirms that the oscillation is primarily confined to a single plane and symmetric, as a circular or elliptical polarization would result in a phase difference of approximately 90°. That is to say, the phase relationship between v_{POS} and v_{LOS} indicates the loop is linearly polarized.

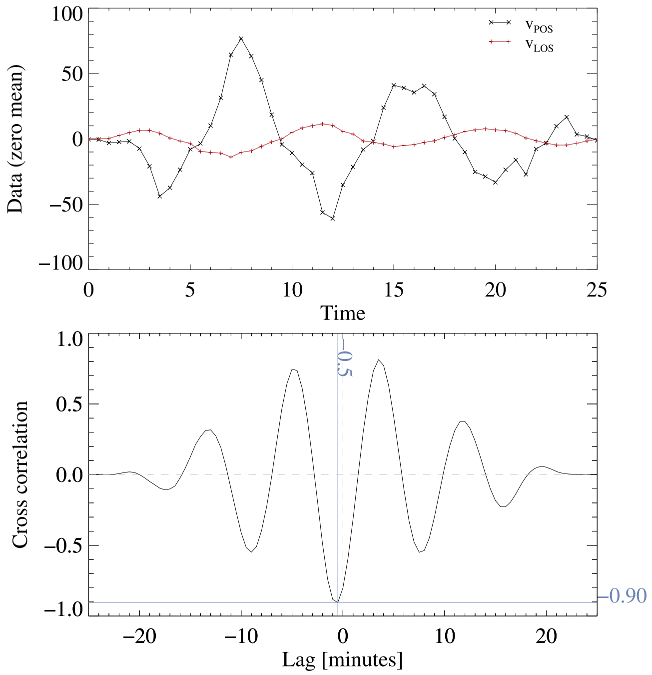

Figure 6. (Top) Comparison of line-of-sight Doppler velocity (v_{LOS}, red) with the transverse velocity in the plane of sky (v_{POS}, black), derived from the derivative of displacement. (Bottom) Cross correlation of v_{LOS} against v_{POS}. Clearly the two velocity curves are in antiphase. The clear monochromatic sinusoid shows there is a common periodicity of ~8.6 minutes, and there is a very strong correlation coefficient value of 0.89.

The Morlet wavelet cross-spectrum and coherence plots, shown in Figure 7, confirm these results. The cross-power spectrum reveals a single dominant periodicity of 515 s, which emerges shortly after the eruption enters the CoMP field of view (at approximately 390 s) and subsequently exhibits damping. The coherence at this frequency is exceptionally high, indicating a strong and consistent relationship between the signals over time. The phase arrows overlaid on both spectra confirm a steady phase relationship between the signals, at approximately 150°.

In contrast to the cross correlation that provides a time-averaged value, the wavelet cross spectrum provides a time-resolved view of the phase relationship, allowing us to track how the phase between LOS and POS velocities evolves over the duration of the oscillation. A deviation of the observed phase difference in the cross spectrum from 180° (or 0°, depending on the convention of v_{POS}) suggests the influence of resonant absorption. As energy is transferred from the global kink mode to the local Alfvén continuum modes, the flux tube's motion changes from a purely transverse oscillation to one with an increasingly significant azimuthal component, as shown analytically by M. Goossens et al. (2014) and numerically by P. Antolin et al. (2017). This process introduces an additional phase offset between the azimuthal and radial velocities, which is then projected onto the POS and LOS, resulting in the observed phase difference. This provides further evidence that resonant absorption may be the dominant damping mechanism in coronal loop kink oscillations, reinforcing previous results that showed how the quality factors for multiple harmonics agree (as expected from resonant absorption; T. J. Duckenfield et al. 2019), which is further substantiated by theoretical considerations (e.g., M. S. Ruderman & R. Erdélyi 2009; M. Guo et al. 2020; R. J. Morton et al. 2021).

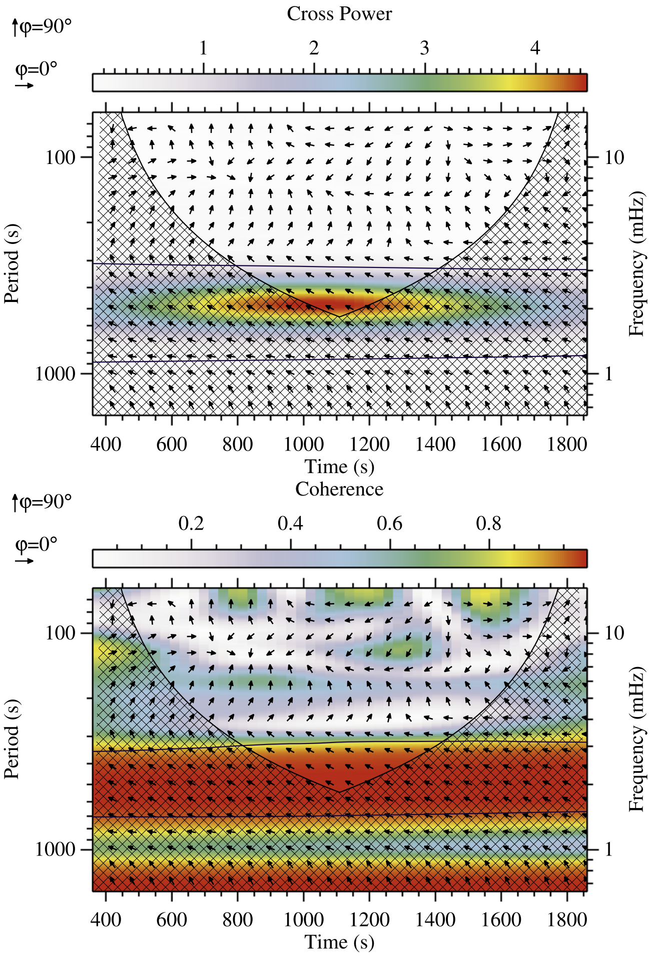

Figure 7. Wavelet cross spectrum (top) and coherence (bottom) calculated between the plane-of-sky velocity and the line-of-sight velocity. The phase angle is depicted by arrows, where pointing directly left means at an 180° angle. The gray hashed lines indicate the cone of influence. The blue contours show the 95% confidence level calculated with a significance test using 1000 random permutations.

3.3. Interpretation of Hodogram: Polarization

Hodograms provide a powerful visualization of oscillatory motion by plotting velocity components against each other, revealing the polarization state and underlying geometry of the oscillation (e.g., S. Zhong et al. 2023; W. Bate et al. 2024). Plotting the velocity vector for this loop oscillation ($v_{\rm POS}$, $v_{\rm LOS}$) with time (Figure 8) reveals a remarkably linear phase portrait, even without any filtering, and confirms that the loop oscillation is linearly polarized. The angle of the hodogram, assuming negligible radial velocity, indicates the orientation of the oscillation in the plane of motion, specifically that the loop sways toward the Sun's southern pole as Earth sees it ($v_{\rm POS} < 0\,\mathrm{km\,s^{-1}}$) while simultaneously moving away from the observer ($v_{\rm LOS} > 0\,\mathrm{km\,s^{-1}}$). Subsequently, as the loop returns back to its equilibrium point, it moves azimuthally toward the solar north and toward the observer. The shallow angle tells us that the plane of oscillation is closely aligned to the POS.

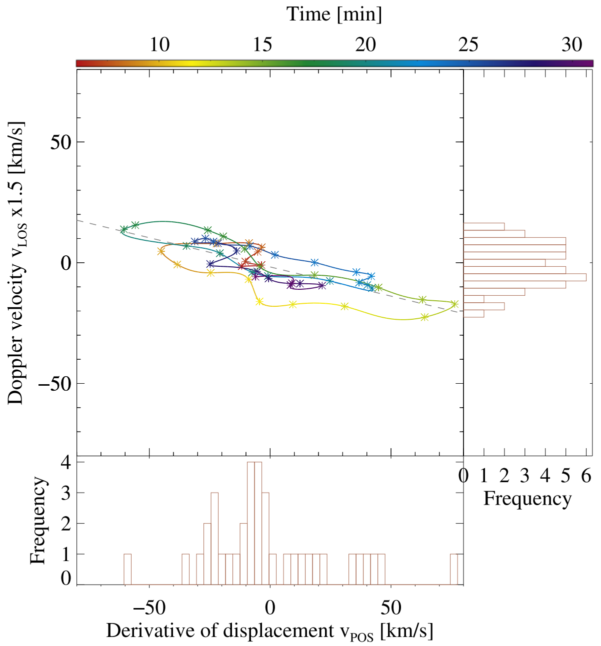

(a) Hodogram

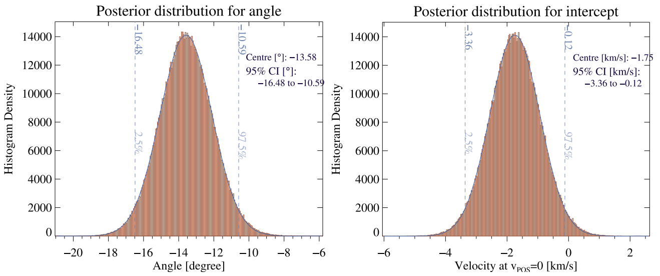

(b) Posterior for angle (c) Posterior for intercept

Figure 8. (a) Hodogram showing the evolution of the velocity vector with time. The plane-of-sky velocity derived from the derivative of the fitted displacement is shown along the *x*-axis, and the Doppler (line-of-sight) velocity extracted by tracking the feature, scaled by ×1.5, is shown along the *y*-axis. The loop's velocity vector, as visualized in the velocity-space hodogram, oscillates along a line oriented at $-13\overset{\circ}{.}6$ relative to the plane of sky. The oscillation can be seen in the animation of the hodogram, which shows the sequence between 6 and 31 minutes. The real-time duration of the animation is 10 s. The bottom panels show normalized histograms approximating the marginalized posterior distributions of the (b) angle and (c) intercept obtained from 10^5 MCMC samples using the model $v_{\rm LOS} = \tan(\mathrm{angle}) * v_{\rm POS} + \mathrm{intercept}$.

(An animation of this figure is available in the online article.)

As mentioned, assuming zero radial displacement and fitting a line of best fit to the hodogram of $v_{\rm LOS}$ versus $v_{\rm POS}$ provides a direct measure of the orientation of the oscillation plane, as the velocities are constrained to the azimuthal and LOS directions. We correct for the known underestimation of Doppler velocities by CoMP through multiplying $v_{\rm LOS}$ by a factor of ×1.5 based on J.-O. Lee et al. (2021) and discussed in Section 2.1. Using the corrected $v_{\rm LOS}$, the line of best fit for the hodogram in Figure 8 is computed with the Bayesian methodology of SoBaT (S. A. Anfinogentov et al. 2021). For the angle variable, a uniform prior $\mathcal{U}(-180°, 180°)$ is used, since we have no expectation for a specific polarization plane. For the intercept variable, a normal prior $\sim\mathcal{N}(0, \sigma_v)$ was used since we expect no bulk motion besides our uncertainty in both velocities, which we (significantly) overestimate using the standard deviation of both $v_{\rm LOS}$ and $v_{\rm POS}$, $\sigma_v \approx 22\,\mathrm{km\,s^{-1}}$. The line of best fit of the hodogram of Figure 8 is found to be

$$v_{\rm LOS} = \tan\left(-13\overset{\circ}{.}6^{+2.9}_{-3.0}\right) * v_{\rm POS} - 1.77^{+1.59}_{-1.65}\ [\mathrm{km\,s^{-1}}],$$

where the error ranges given are for the 95% confidence interval. Testing showed the results were insensitive to the choice of priors. The bottom panels (b) and (c) of Figure 8 show the well-constrained marginalized posterior distributions for the angle and intercept, estimated by 10^5 MCMC samples.

4. Discussion

Reiterating the assumption of zero radial displacement, its phase behavior suggests the kink oscillation in this study is linearly polarized and oscillating in a plane approximately 14° tilted from the POS, such that the loop apex alternates between moving away from Earth and azimuthally southward, and moving toward Earth and azimuthally northward. Note that the calculations of cross correlation, cross spectrum, and coherence are primarily sensitive to the phase relationship between v_{LOS} and v_{POS} and are thus unaffected by any underestimation of velocity amplitudes. No matter the level to which v_{LOS} is underestimated, the linear polarization of the kink oscillation remains, though the resultant angle of the plane of oscillation would be different. The same calculation for v_{LOS} without scaling yields an angle of $9\overset{\circ}{.}2^{+2.1\circ}_{-2.0}$ and an intercept of $-1.2^{+1.1}_{-1.1}$ km s^{-1}.

The nonzero intercept of the line calculated for the hodogram in Figure 8 may imply some bulk motion of the loop, in this case toward the observer at approximately 2 km s^{-1}. Note that the CoMP Level 2 FITS files have been corrected for solar rotation effects, at least partially. A smoothed polynomial fit, combined with a zero-median assumption for each frame, was used to adjust the Doppler velocity measurements, accounting for the blueshift at the east limb and redshift at the west limb (S. Tomczyk et al. 2022). Nonetheless, this small bulk velocity could be a residual from the solar rotation.

4.1. Line Widths

As with the Doppler velocities, by precisely tracking the loop as it moves, we can extract the line width from its apex. Referring to Figure 9, there is a clear periodic increase in line width as the loop oscillates. Curiously, the line widths appear broadened throughout the entire loop, giving credibility. The line width enhancement is at a maximum when v_{LOS} is at its most negative (blueshifted) and v_{POS} is at its greatest (i.e., when the inhomogeneity is passing through its equilibrium point). The dominant period matches that of the kink oscillation, 8 minutes; however, a peak at the double frequency is also above the 95% confidence level. It is expected that a peak at twice the frequency is related to two wave maxima being present during each complete oscillation. Previously, this type of behavior has been attributed to unresolved line width fluctuations synonymous with torsional Alfvén waves (e.g., D. B. Jess et al. 2009; M. Mathioudakis et al. 2013). Furthermore, P. Antolin et al. (2017) attributed this to large shear flows at the boundary layer of the loop, which subsequently induce eddies and instabilities that appear as spectral line broadening when unresolved. As these shear flows are greatest as the loop reaches its maximum speed regardless of the direction of motion, the period of line enhancements is expected to be doubled. There is also a remote possibility that the line width increase is due to the thermalization of the plasma, increasing the thermal width. The exact mechanism is unclear from this observation alone. Nonetheless, the detection of a double frequency oscillation in line width for an isolated kink oscillation is, to the authors' knowledge, the first of its kind, and will be followed up in a future publication.

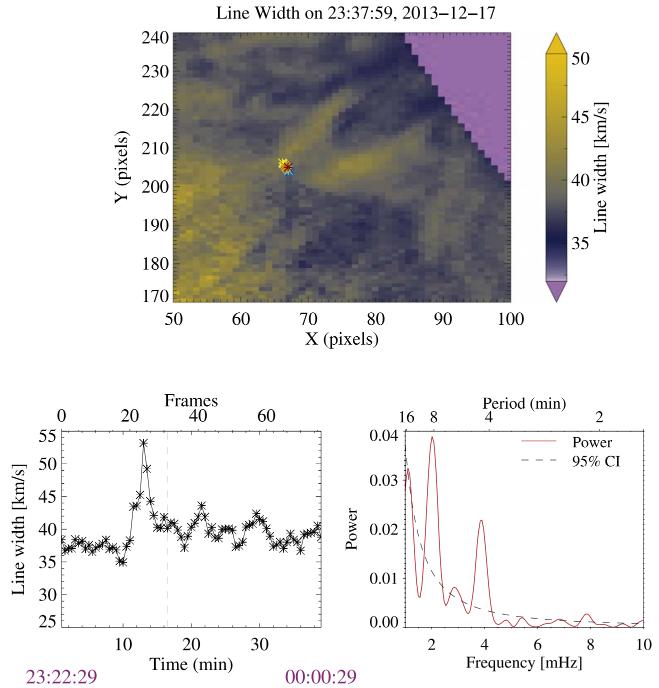

Figure 9. The line width at the loop apex (1.18 $R_\odot$) is tracked as it moves. (Top) The location of the points from which the line width is extracted. (Bottom left) The time series of the line width at loop apex. The vertical dashed line indicates the snapshot displayed above, chosen to best highlight the loop structure. (Bottom right) The power spectrum of the extracted line widths, showing two peaks (2.0 and 3.9 mHz) above the 95% confidence level.

4.2. Outlook

The approach outlined in this work—combining Doppler velocities and POS tracking to infer the polarization of transverse motions in solar structures—can be achieved using a single instrument and has the potential to revolutionize coronal seismology. By systematically supplementing observations of coronal waves with constraints on their polarization, we can better estimate their velocity amplitudes and absolute displacements, which will help seismologists derive more accurate estimates of energy flux and deposition rates. Ultimately quantifying how much energy waves transport, and how they contribute to coronal heating, will bring us closer to resolving the coronal heating problem. Additionally, observing a wave's polarization and how it may change over time provides additional information observers can use to better understand the underlying geometry and dynamics.

In the general case, the inference of polarization may require an analysis of all three velocity components (both POS displacements and Doppler velocity) and their phase relationship, but the principle is unchanged. As demonstrated here, the CoMP is well suited to this technique, and by providing continuous, long-duration observations of the entire corona it enables comprehensive studies of wave polarization (as well as propagation) through the solar corona. Excitingly, the instrument has since been upgraded (it is now referred to as uCoMP) to a larger field of view (previously 1.05–1.3 $R_\odot$, now 1.03–1.95 $R_\odot$); wider spectral range (1074–1083Å, now 530–1083Å); and improved spatial resolution ($4\overset{\prime\prime}{.}5$ pixel^{-1}, now 3″ pixel^{-1}), and it has been taking daily scientific observations since mid-2021.[4] This upgrade will allow

---

[4] Note that an eruption of nearby volcano Maunaloa on 2022 November 28 closed the observatory. Repairs are due to be completed by May 2025.

more precise tracking of transverse motions across a wider range of coronal structures, while the expanded spectral coverage will enable simultaneous analysis of additional lines, improving the accuracy and applicability of the polarization inference technique demonstrated in this paper, something we aim to explore in a future paper.

The upcoming Multi-slit Solar Explorer (MUSE; B. De Pontieu et al. 2020) mission, designed to deliver high-resolution spectroscopy and imaging of the solar corona, will also be able to employ this technique, although there will be some differences. While MUSE's smaller field of view and shorter observation windows limit it to case-by-case studies, its ability to resolve fine spatial and temporal details, along with complementary observations across multiple spectral lines, offers great potential for advancing our understanding of wave dynamics, energy transport, and dissipation.

4.3. Conclusion

This paper introduces a novel method in coronal seismology that combines the tracking of oscillations in the imaged plane with Doppler LOS velocities. By fitting the best-fit angle to the hodogram (or phase portrait) of the oscillation, the polarization can be inferred. For this example using CoMP data, a kink oscillation excited by a small coronal eruption was found to be linearly polarized, oscillating in an azimuthal direction in a plane roughly 14° inclined from the POS. The wavelet cross spectrum showed a small deviation of the phase shift between the Doppler velocity and projected POS velocities, as expected from resonant absorption; the process which, according to theoretical/analytical works, is an efficient mechanism for damping kink waves by transferring their energy into unresolved azimuthal Alfvén waves, which can then dissipate their energy into heating. An intriguing hint of double frequency periodicity was detected in the line width data, which adds to the suggestion of instabilities at the oscillating loop boundary. We anticipate the broad applicability of this hodogram tool to the enhanced observations of the upgraded uCoMP system. The improved spatial and temporal resolution of uCoMP, coupled with its continuous monitoring of the entire corona, increases the likelihood of capturing fortuitous events for detailed study. This enables the widespread study of kink oscillations using a single instrument. Stereoscopy is a timely topic, especially with the wealth of solar observations from missions like Solar Orbiter and MUSE. Hodograms offer a complementary tool for analyzing these stereoscopic data sets. This technique has potential applications to other aspects of coronal science. The relevant codes for the analysis and techniques used in this paper are available through the Waves in the Lower Solar Atmosphere coding repository, WaLSAtools[5] (S. Jafarzadeh et al. 2025). The data used in this study can be provided upon reasonable request to the corresponding author.

Acknowledgments

T.J.D. and D.B.J. thank the Leverhulme Trust for support via the Research Project grant RPG-2019-371. D.B.J. and S.J. wish to thank the UK Science and Technology Facilities Council (STFC) for the consolidated grants ST/T00021X/1 and ST/X000923/1. D.B.J. also acknowledges funding from the UK Space Agency via the National Space Technology Programme (grant SSc-009). R.J.M. is supported by a UKRI Future Leader Fellowship (RiPSAW-MR/T019891/1). Finally, we wish to acknowledge scientific discussions with the Waves in the Lower Solar Atmosphere (WaLSA; https://www.WaLSA.team) team, which has been supported by the Research Council of Norway (project no. 262622), The Royal Society (award no. Hooke18b/SCTM; D. B. Jess et al. 2021), and the International Space Science Institute (ISSI Team 502).

Facilities: HAO (CoMP), SDO (AIA).

ORCID iDs

T. J. Duckenfield https://orcid.org/0000-0003-3306-4978
D. B. Jess https://orcid.org/0000-0002-9155-8039
R. J. Morton https://orcid.org/0000-0001-5678-9002
S. Jafarzadeh https://orcid.org/0000-0002-7711-5397

References

Anfinogentov, S. A., Nakariakov, V. M., Pascoe, D. J., & Goddard, C. R. 2021, ApJS, 252, 11
Antolin, P., Moortel, I. D., Doorsselaere, T. V., & Yokoyama, T. 2017, ApJ, 836, 219
Aschwanden, M. J., & Schrijver, C. J. 2011, ApJ, 736, 102
Ballai, I., Jess, D. B., & Douglas, M. 2011, A&A, 534, A13
Bate, W., Jess, D. B., Grant, S. D. T., et al. 2024, ApJ, 970, 66
Duckenfield, T. J., Goddard, C. R., Pascoe, D. J., & Nakariakov, V. M. 2019, A&A, 632, A64
De Pontieu, B., Martïnez-Sykora, J., Testa, P., et al. 2020, ApJ, 888, 3
Goossens, M., Andries, J., & Aschwanden, M. J. 2002, A&A, 394, L39
Goossens, M., Soler, R., Terradas, J., Doorsselaere, T. V., & Verth, G. 2014, ApJ, 788, 9
Guo, M., Li, B., & Doorsselaere, T. V. 2020, ApJ, 904, 116
Jafarzadeh, S., Jess, D. B., Stangalini, M., et al. 2025, Nature Reviews Methods Primers, in press
Jess, D. B., Jafarzadeh, S., Keys, P. H., et al. 2023, LRSP, 20, 1
Jess, D. B., Keys, P. H., Stangalini, M., & Jafarzadeh, S. 2021, RSPTA, 379, 20200169
Jess, D. B., Mathioudakis, M., Erdélyi, R., et al. 2009, Sci, 323, 1582
Lee, J.-O., Lee, K.-S., Seough, J., & Cho, K.-S. 2021, JKAS, 54, 49
Long, D. M., Valori, G., Pïrez-Suïrez, D., Morton, R. J., & Vïsquez, A. M. 2017, A&A, 603, A101
Magyar, N., Duckenfield, T., Doorsselaere, T. V., & Nakariakov, V. M. 2022, A&A, 659, A73
Mathioudakis, M., Jess, D. B., & Erdélyi, R. 2013, SSRv, 175, 1
McIntosh, S. W., & Pontieu, B. D. 2012, ApJ, 761, 138
Moortel, I. D., & Pascoe, D. J. 2012, ApJ, 746, 31
Morton, R. J., Tiwari, A. K., Doorsselaere, T. V., & McLaughlin, J. A. 2021, ApJ, 923, 225
Morton, R. J., Tomczyk, S., & Pinto, R. 2015, NatCo, 6, 7813
Nakariakov, V. M., Anfinogentov, S. A., Antolin, P., et al. 2021, SSRv, 217, 73
Nakariakov, V. M., Zhong, S., Kolotkov, D. Y., et al. 2024, RvMPP, 8, 19
Pant, V., Magyar, N., Doorsselaere, T. V., & Morton, R. J. 2019, ApJ, 881, 95
Pascoe, D. J., Goddard, C. R., Nisticó, G., Anfinogentov, S., & Nakariakov, V. M. 2016, A&A, 589, A136
Podladchikova, O., Harra, L., Barczynski, K., et al. 2021, A&A, 655, A57
Ruderman, M. S., & Erdélyi, R. 2009, SSRv, 149, 199
Sharma, R., & Morton, R. J. 2023, NatAs, 7, 1301
Tomczyk, S., Card, G. L., Darnell, T., et al. 2008, SoPh, 247, 411
Tomczyk, S., Landi, E., Berkey, B., et al. 2022, BAAS, 54, 2022n7i205p01
Verwichte, E., Aschwanden, M. J., Doorsselaere, T. V., Foullon, C., & Nakariakov, V. M. 2009, ApJ, 698, 397
Yang, Z., Bethge, C., Tian, H., et al. 2020, Sci, 369, 694
Yang, Z., Tian, H., Tomczyk, S., et al. 2024, Sci, 386, 76
Zhong, S., Nakariakov, V. M., Kolotkov, D. Y., et al. 2023, NatCo, 14, 5298
Zimovets, I. V., & Nakariakov, V. M. 2015, A&A, 577, A4

---

[5] WaLSAtools website: https://WaLSA.tools.